



# Multiobjective design optimization of stent geometry with wall deformation for triangular and rectangular struts

Narendra Kurnia Putra<sup>1</sup> · Pramudita Satria Palar<sup>2</sup> · Hitomi Anzai<sup>2</sup> · Koji Shimoyama<sup>2</sup> · Makoto Ohta<sup>2</sup>

Received: 16 November 2017 / Accepted: 18 June 2018 / Published online: 2 July 2018  
© International Federation for Medical and Biological Engineering 2018

## Abstract

The stent geometrical design (e.g., inter-strut gap, length, and strut cross-section) is responsible for stent–vessel contact problems and changes in the blood flow. These changes are crucial for causing some intravascular abnormalities such as vessel wall injury and restenosis. Therefore, structural optimization of stent design is necessary to find the optimal stent geometry design. In this study, we performed a multiobjective stent optimization for minimization of average stress and low wall shear stress ratio while considering the wall deformation in 3D flow simulations of triangular and rectangular struts. Surrogate-based optimization with Kriging method and expected hypervolume improvement (EHVI) are performed to construct the surrogate model map and find the best configuration of inter-strut gap ( $G$ ) and side length ( $SL$ ). In light of the results,  $G$ - $SL$  configurations of 2.81–0.39 and 3.00–0.43 mm are suggested as the best configuration for rectangular and triangular struts, respectively. Moreover, considering the surrogate model and flow pattern conditions, we concluded that triangular struts work better to improve the intravascular hemodynamics.

**Keywords** Restenosis · Stent · Computational simulation · Multiobjective optimization · Kriging surrogate method

## 1 Introduction

Restenosis is the reoccurrence of stenosis or blockage on post-stented blood vessels [1]. Restenosis has been reported in one in ten patients with drug-eluted stents (DES) [2] and up to one-third of the patients with bare metal stents (BMSs) [1]. To the best of our knowledge, restenosis is induced by the mechanical and hemodynamic interactions between the stent and blood vessel. From a mechanical perspective, the stent–vessel contact may lead to cell inflammation owing to vessel injury problems [3, 4]. Moreover, the stent expansion deforms the vessel walls and may alter the flow around the strut [5, 6]. Then, changes in the flow pattern and orientation occur owing to flow obstruction because of the stent implantation [7–10]. When undesirable hemodynamic conditions occur (i.e., big recirculation zone),

atherogenesis develops owing to low wall shear stress (WSS) causing restenosis. The stent geometrical design (e.g., porosity, length, and strut cross section) is responsible for stent–vessel contact problems and changes in the flow orientation [11, 12]. Consequently, many studies have concentrated on minimizing the undesirable effects of stent implantation.

Stent structural optimization studies have been performed to find the ideal stent configuration based on mechanical or hemodynamic objectives [13–19]. Srinivas et al. first optimized stents with different strut configurations to minimize vorticity and maximize WSS [13]. In contrast, studies on the strut cross sections suggest that alternative streamlined strut shapes offer improved stent performance [11, 12, 20]. Mejia et al. showed that streamlined shape stent struts are likely to reduce the occurrence of flow disturbance [11]. The experimental study by Chen et al. suggested that cells behave differently when different strut shapes are used; thus, the optimization of the cross-sectional shape of stent wires is necessary [12].

Recent optimization of the stent design for intravascular treatment targets mostly single objective or physical phenomena (i.e., flow dynamics or structural mechanics) [15, 17, 18, 21]. The review by Bressloff et al. covered the optimization of coronary stent systems and proposed future optimization targets, such as the WSS that strongly affects the endothelial cell

✉ Narendra Kurnia Putra  
naren@biofluid.ifs.tohoku.ac.jp

<sup>1</sup> Department of Bioengineering and Robotics, Graduate School of Engineering, Tohoku University, Aramaki-Aza Aoba 6-6-4, Aoba-ku, Sendai, Miyagi 980-8579, Japan

<sup>2</sup> Institute of Fluid Science, Tohoku University, Katahira 2-1-1, Aoba-ku, Sendai, Miyagi 980-8577, Japan

activity [16]. Therefore, further optimization studies of fluid and structural mechanics using clinically or biologically focused objective functions are needed. To date, we performed single objective optimization based on the surrogate method and 2D axis-symmetrical stent models to minimize the low WSS area [22, 23]. We found that the surrogate model offers improvement on computational efficiency and design.

This study examines multiobjective stent optimization by minimizing mechanical and biological flow dynamics parameters and considering the wall deformation in 3D flow simulations of simple ring-shaped stents. The simulation was based on the finite-element method with high computational cost. Therefore, the surrogate-based optimization framework has been selected because the direct optimization of complex physical systems is time-consuming [24]. Basically, surrogate-based optimization predicts the objective function and then uses it as the metamodel of the physical system in the simulations [25]. By using the surrogate model, predictions of the objectives and research processes of the optimized design are efficiently performed. Besides, we also compare the optimized performance for different cross-sectional shapes on minimizing the objectives.

## 2 Methods

### 2.1 Design variables and sampling strategy

Finding the best configuration of inter-strut gap length ( $G$ ) and side length ( $SL$ ) configuration is the main purpose of this work with the general framework is shown in Fig. 1. For accurate observation, a sufficient sample set is necessary. Twenty-six samples of  $G$ - $SL$  combinations were generated by the Halton sampling method for each strut shape. As previously explained on our work [23], the Halton sampling points were obtained by pairing two sets of mutually prime-based Halton sequences in a unit square [26]. These sequences can be obtained for any  $m$ -th Halton number firstly within 0 to 1 intervals by

$$H_m(b) = \frac{d_0}{b} + \frac{d_1}{b^2} + \frac{d_2}{b^3} + \dots + \frac{d_j}{b^{j+1}}, \quad (1)$$

where  $m$  is any integer, which is written in the base- $b$  notation of

$$m = d_0 + d_1b + d_2b^2 + \dots + d_jb^j. \quad (2)$$

For this sample generation, we used pairs of Halton sequences based on 2 and 3. Afterwards, normalization was performed to fit to our  $G$ - $SL$  configurations that were generated for  $G$  between 1 and 3 mm and  $SL$  between 0.05 and 0.45 mm. This sampling strategy has been used to obtain the “space-filling” distribution along the sampling range. In

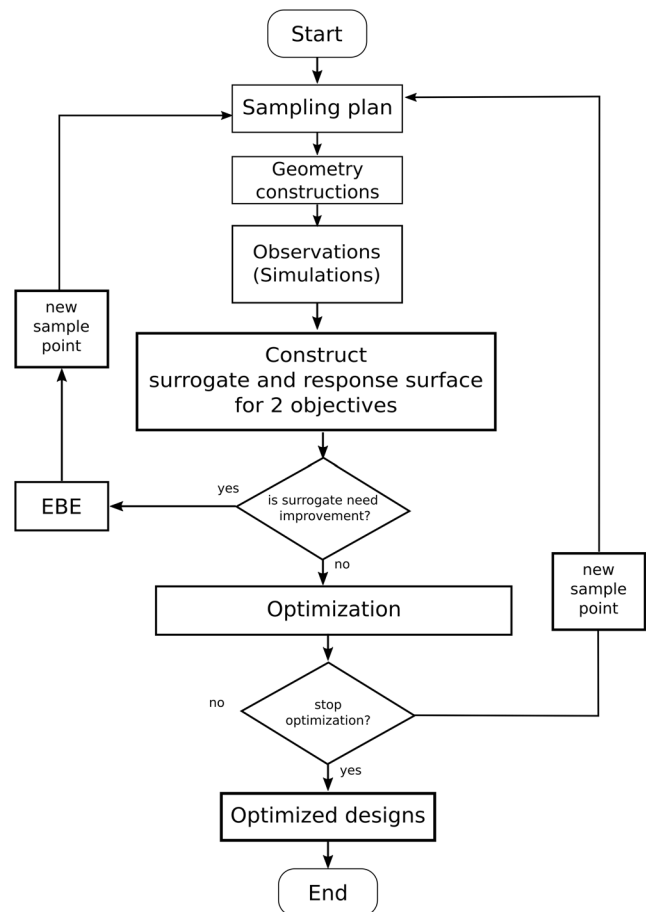


Fig. 1 Optimization flow chart

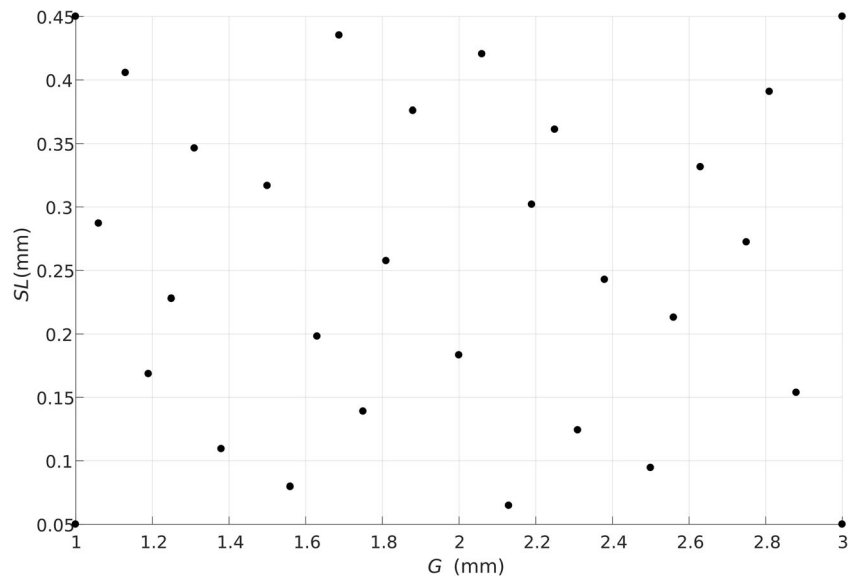
addition to these 26 samples (Fig. 2), more points were added to the dataset when necessary.

### 2.2 Geometry construction

The wall deformation in post-stented blood vessels was observed in in vivo studies [5, 27]. Moreover, studies show the parent artery expansion and straightening due to stent deployment based on the in vivo vessel reconstructions. These works also suggest that the inflow and hemodynamic properties change owing to the alteration of post-stented blood vessel geometry [10, 28–30]. Therefore, it is necessary to include the wall deformation in the simulation. To obtain the deformed geometry and investigate the effect of this deformation to the flow condition, the following two consecutive simulations were performed: structural mechanics and solid-flow coupled simulation (Fig. 3). The 4-mm blood vessel diameter geometry settings are shown in Fig. 4 along with the design variables for the different strut cross-sectional shapes,  $G$ , and  $SL$ . Rectangular struts are typical laser-cut stents, while triangular struts are proposed as streamlined strut shapes.

Geometry creation was begun with obtaining the desired blood vessel deformation by applying 5.5% displacement for

**Fig. 2** Initial sample set obtained from the Halton sequence method



all stent geometries [5]. Once the deformed geometry was obtained, it was taken as the initial wall geometry in the fluid flow simulation. Afterwards, the wall geometry is rotated to obtain the symmetrical 3D geometry of the deformed blood vessel. The new cylindrical geometry was added followed by Boolean operations to add the flow domain on the central part of the vessel body. Finally, the geometry was divided into four symmetrical parts to reduce the computational cost.

### 2.3 Boundary and simulation settings

The stent struts are defined as NiTi material with Young’s modulus and Poisson’s ratio of 80 GPa and 0.33, respectively [31]. The Young’s modulus and Poisson’s ratio of the blood vessel layer and muscle tissues are 0.7 GPa and 0.45 for the

no-slip wall vessel layer and 1.16 MPa and 0.45 for the muscle tissue [32, 33]. In the fluid domain, the blood was assumed to be an incompressible Newtonian fluid with a viscosity of 3.5 mPa·s and density of 1050 kg m<sup>-3</sup> [34].

The flow boundary condition was that of stationary laminar inflow with a mean velocity of 0.33 ms<sup>-1</sup> and 0 Pa laminar outflow boundary condition. The flow boundary condition corresponds to Reynolds number of 396 [13]. In addition, along the flow–vessel boundary, static pressure of 100 mmHg from the average normal human blood pressure and dynamic pressure from flow phenomena were set as fluid–solid coupled boundary loads to test if any wall deformation occurs. All simulation steps and boundary condition settings were the same as well as both strut cross-sectional shapes. Triangular and hexagonal meshes were used in the mechanical and fluid

**Fig. 3** Details of simulation procedures as observation step to construct the surrogate model

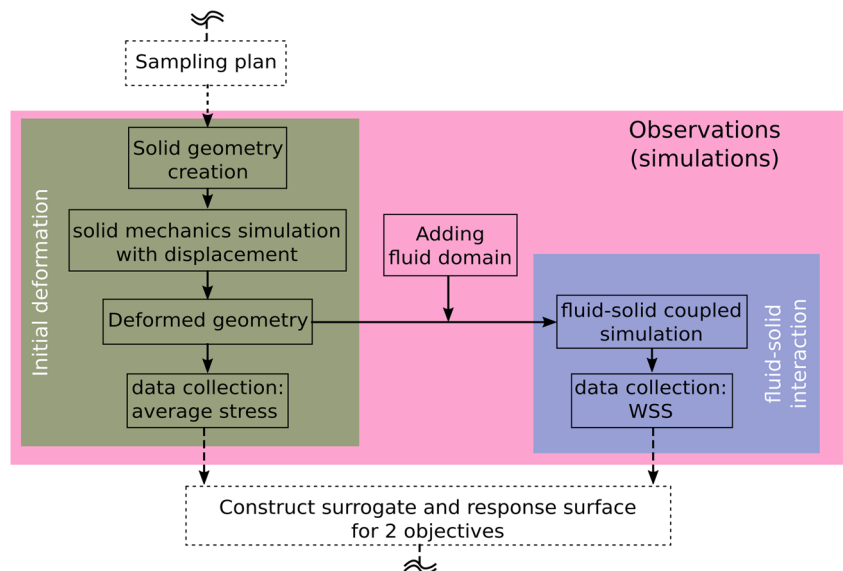
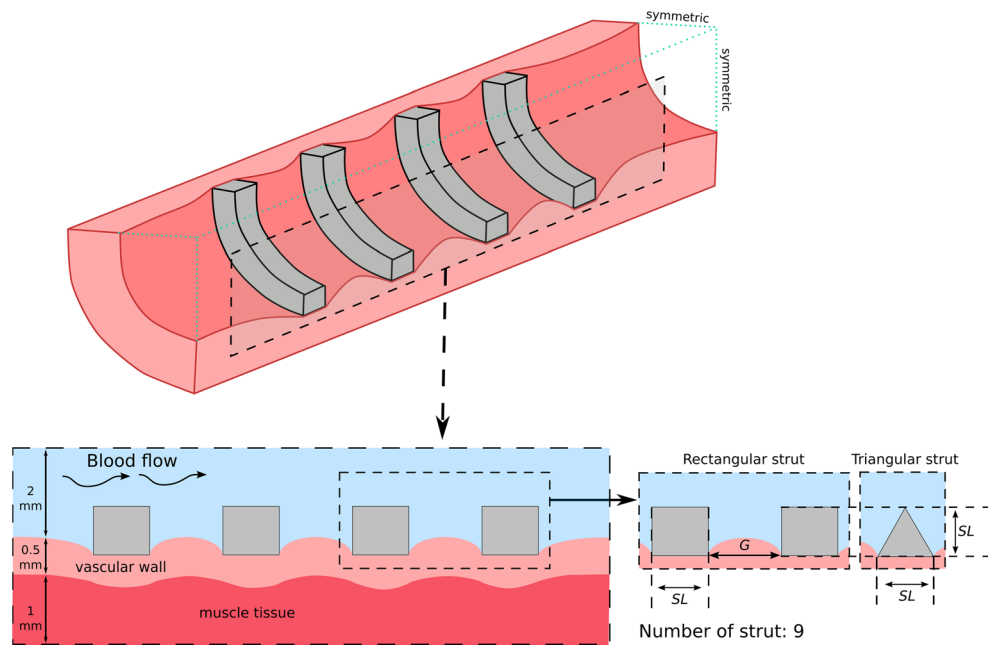


**Fig. 4** Model geometry and dimensional settings



simulations. A mesh dependency test was performed for each representative case of both mechanical stress and fluid–solid coupled simulation with the solution converged within 1% (Fig. 5). Similar mesh quality criteria were maintained for all simulations during the optimization process.

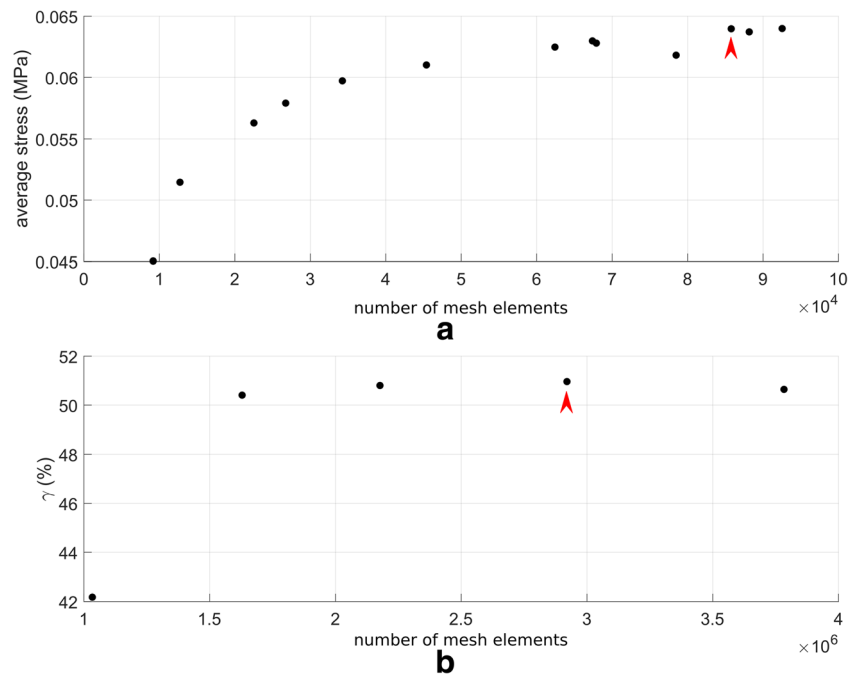
The simulations were performed using COMSOL Multiphysics 5.0 (Comsol Inc., Stockholm, Sweden) with structural mechanics and laminar flow coupled systems. This simulation is performed in two consecutive steps, as shown in Fig. 3. The solid domain parts were defined as linear elastic materials that work based on the equation of motion with

strain displacement equation based on Young’s modulus and Poisson’s ratio. The fluid domain parts were considered to belong to laminar flow by solving the Navier–Stokes equation. Interaction between deformation and stress normal work based on Cauchy stress which formulated as the pressure and viscous terms in Navier–Stokes, read as

$$\sigma \cdot \mathbf{n} = (-\nabla P + \mu \nabla^2 \mathbf{V} + \rho \mathbf{g}) \cdot \mathbf{n}, \tag{3}$$

where  $\mathbf{n}$  is the normal vector,  $P$  is pressure,  $\mu$  is the viscosity,  $\mathbf{V}$  is blood velocity,  $\rho$  is the blood density, and  $\mathbf{g}$  is the body

**Fig. 5** Mesh dependency results for both simulation steps: **a** initial deformation simulation and **b** fluid–solid coupled simulation. Points with red arrow indicate the mesh number used in the simulation



acceleration or gravity. The convergence criteria were set to a maximum residual of  $10^{-5}$ .

### 2.4 Design variables and objective functions

The endothelial cells on the blood vessel surface are greatly affected by the WSS conditions [7–9, 13, 35]. Low WSS (WSS < 0.5 Pa [7, 8]) is possibly the major reason for restenosis owing to cell migration and platelet activations. Therefore, we used the parameter of low WSS ratio ( $\gamma$ ) (< 0.5 Pa), which appears on the blood vessel surface. The detail calculation of  $\gamma$  has been discussed previously [23]. Besides WSS, mechanical stress owing to stent deployment is also critical to the vessel wall conditions because of inflammation and cell traumas.

The average stress in the post fluid–solid coupled simulation is obtained at infinitesimal values compared to the initial deformation. Therefore, this parameter is neglected in the analysis which is also in line with previous work [36]. The minimization of  $\gamma$  and the initial average stress due to the wall deformation are chosen as the objective functions.

### 2.5 Surrogate model construction and accuracy improvement method

The simulated system has been treated as a black box and finding the system’s objective function  $f(x)$  analytically is difficult; therefore, we chose the surrogate optimization method based on Kriging to estimate the objective function ( $\hat{f}(x)$ ) by generating random Gaussian functions and interpolating the responses [25, 37]. Next, the estimated objective function is used in the optimization steps. Moreover, surrogate model maps of the objective function are constructed. The surrogate model map is used to observe the effect of the stent design configuration and improve the stent design. The surrogate model and optimization code used in this study were developed by the Aerospace Fluid Engineering Laboratory, Institute of Fluid Science of Tohoku University.

Error-based exploration was performed to further refine the surrogate model. This method basically tries to minimize the

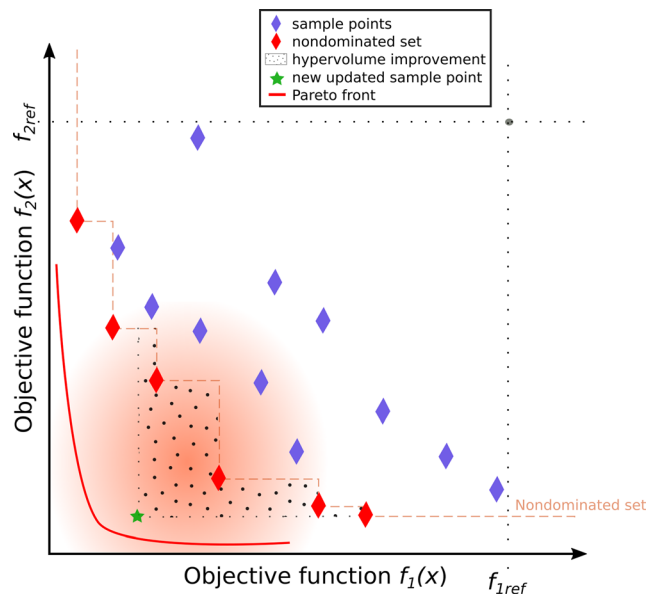


Fig. 6 Nondominated set of points and EHVI method

Kriging error by suggesting new sample points with the highest predictor error values [25]. New simulations are then performed for the new sample point and the surrogate model is updated.

### 2.6 Multiobjective optimization and the expected hypervolume improvement method

Realistic optimization frequently features a trade-off between two and more objectives. Multiobjective optimization approach is necessary to handle problems with conflicting objectives. A Pareto optimal set is the collection of solutions in which an improvement in one objective cannot be optimized without degrading the other objectives [38]. Therefore, the proposed optimization aims to find the Pareto optimal solutions with  $\gamma$  and initial average stress as the objectives.

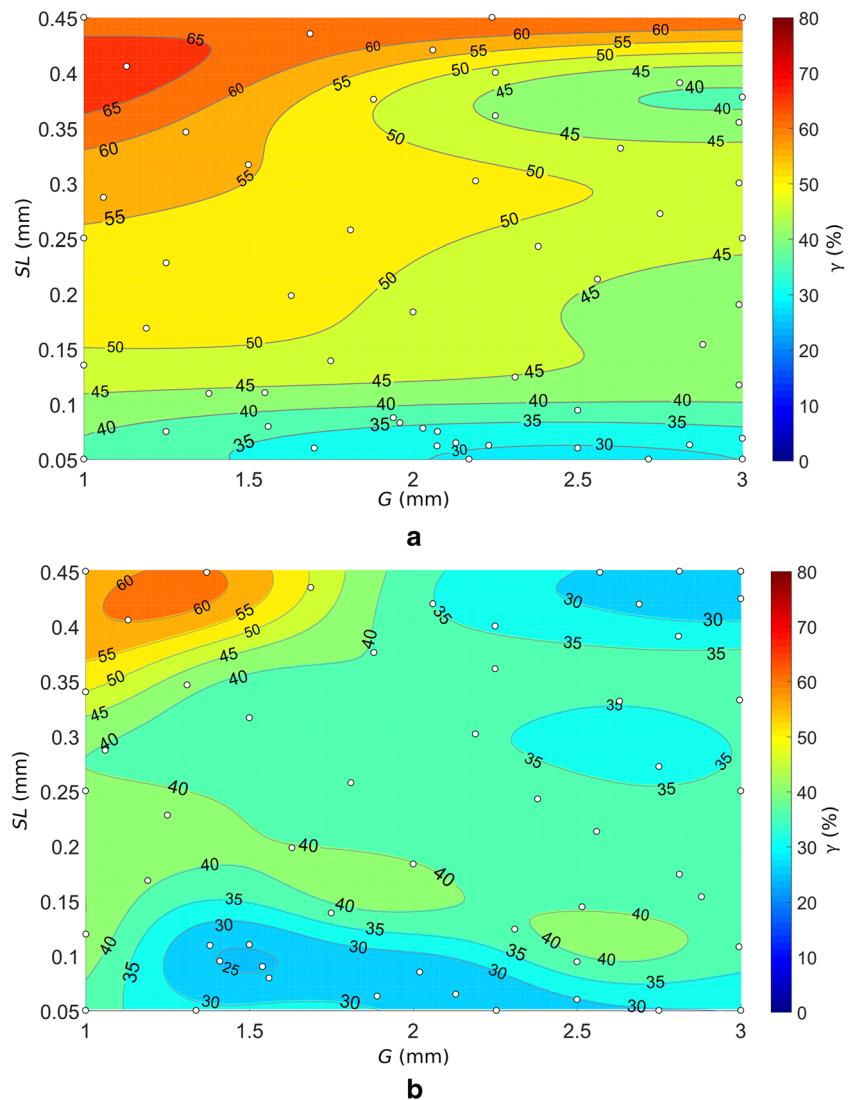
The EHVI method [39] was adopted as the multiobjective optimization algorithm. EHVI is based on the difference of the hypervolume between two sample sets of the Kriging model (Fig. 6). The EHVI is defined as

$$EHVI[f_1(x), f_2(x), \dots, f_m(x)] = \int_{-\infty}^{f_{1ref}} \int_{-\infty}^{f_{2ref}} \dots \int_{-\infty}^{f_{mref}} HVI[f_1(x), f_2(x), \dots, f_m(x)] \times \phi_1(F_1) \cdot \phi_2(F_2) \dots \phi_n(F_m) dF_1 dF_2 \dots dF_m \tag{4}$$

where  $f_i$  is the Gaussian random variable,  $\phi_i(F_i)$  is the probability function, and  $f_{iref}$  the hypervolume reference value [38]. The samples are enriched so that subsequent samples move closer to the Pareto front. Hypervolume is defined as the

volume enclosed by the current nondominated solutions and the defined reference point for the hypervolume calculation. For a given reference point, the solutions that yield the highest hypervolume belong to the Pareto optimal set (Fig. 6). Each

**Fig. 7** Surrogate model for  $\gamma$  for **a** rectangular and **b** triangular stent struts



update of EHVI tries to find a solution that improves the hypervolume of the current nondominated set, hence the concept of hypervolume improvement.

### 3 Results

From the simulation, we obtain the response data for each  $\gamma$  and the average mechanical stress along the deployment area. Fifty-four different design configurations were simulated for each strut shape. The average computational time for each rectangular and triangular shape is 39 min and 16 s and 26 min and 30 s, respectively, excluding meshing and pre- and post-processing.

#### 3.1 Rectangular stent: Kriging surrogate models

Two surrogate models were obtained for each objective function:  $\gamma$  (Fig. 7) and average stress (Fig. 8). As shown

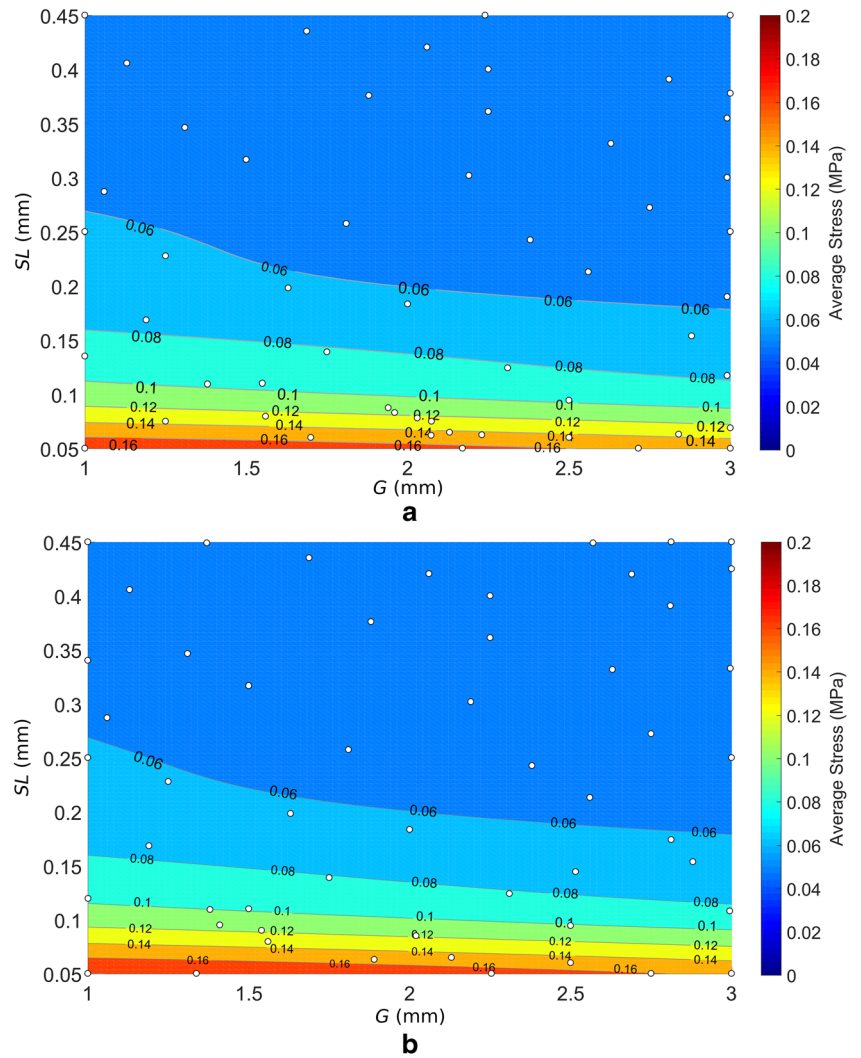
in Fig. 7, the system response based on each  $G$  and  $SL$  ( $G$ - $SL$ ) configuration shows the global increment in  $\gamma$  with increasing  $SL$ . The lowest rate of  $\gamma$  (%) is predicted to occur in the  $G$  range of 2.1–3 mm and  $SL$  less than 0.07 mm. Several interesting areas of low  $\gamma$  are obtained for  $G$  greater than 2 mm and different  $SL$ . Further investigations of the flow conditions under these particular configurations will be discussed in the Section 4.

In the average stress minimization case, the  $SL$  increase causes the average stress to decrease. Such behavior occurs for struts with  $SL$  greater than 0.2 mm and rapid increments are noticed under this size.

#### 3.2 Triangular stent: Kriging surrogate models

The surrogate model in Fig. 7b suggests that generally lower  $\gamma$  values are obtained by the triangular strut. High  $\gamma$  values are associated with small  $G$  and large  $SL$ . On the other hand, low  $\gamma$  areas are observed under several

**Fig. 8** Surrogate model contour map for average stress on **a** rectangular and **b** triangular stent struts

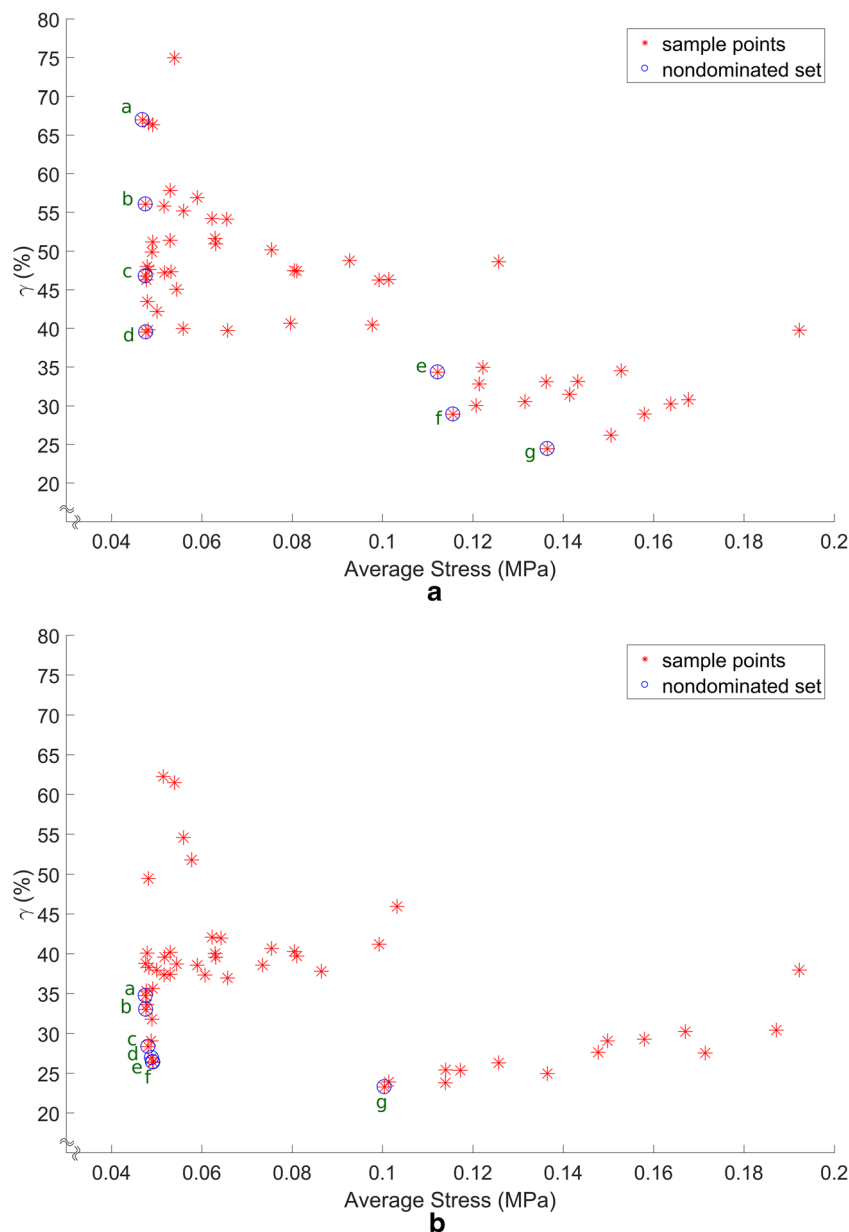


design configurations, i.e., along small  $SL$ , long  $G$  and medium  $SL$ , and long  $G$  and large  $SL$ . The lowest  $\gamma$  values are concentrated and are associated with small to medium  $G$ .

**Table 1** Nondominated points

	Point	$G$ (mm)	$SL$ (mm)	$\gamma$ (%)	Average stress (MPa)	Case
Rectangular strut	a	2.24	0.45	66.97	0.047	36
	b	2.06	0.42	56.05	0.048	17
	c	2.25	0.36	46.78	0.048	5
	d	2.81	0.39	39.51	0.048	23
	e	1.94	0.09	34.33	0.112	49
	f	1.96	0.08	28.92	0.116	50
	g	2.13	0.06	24.44	0.136	9
Triangular strut	a	2.06	0.42	34.72	0.048	17
	b	2.81	0.39	33.02	0.048	23
	c	2.69	0.42	28.35	0.048	51
	d	2.81	0.45	26.94	0.049	44
	e	3.00	0.45	26.43	0.049	30
	f	3.00	0.43	26.39	0.049	49
	g	1.50	0.11	23.27	0.100	48

**Fig. 9** Nondominated set of points for **a** rectangular and **b** triangular stent struts



With respect to the second objective (Fig. 8b), general behavior is similar to that of the rectangular strut is observed. These results suggest that large struts minimize the average stress along the deployment area. Generally, we observed that there is a trade off between the two objectives. Therefore, multiobjective optimization is necessary.

### 3.3 Multiobjective solutions: nondominated point set

The set of multiobjective solutions is given in Table 1 and shown in Fig. 9. Seven nondominated points were obtained for rectangular and triangular struts after 14 and 12 EHVI iterations, respectively. The final optimal design is chosen after considering each point of interest in the analysis. The

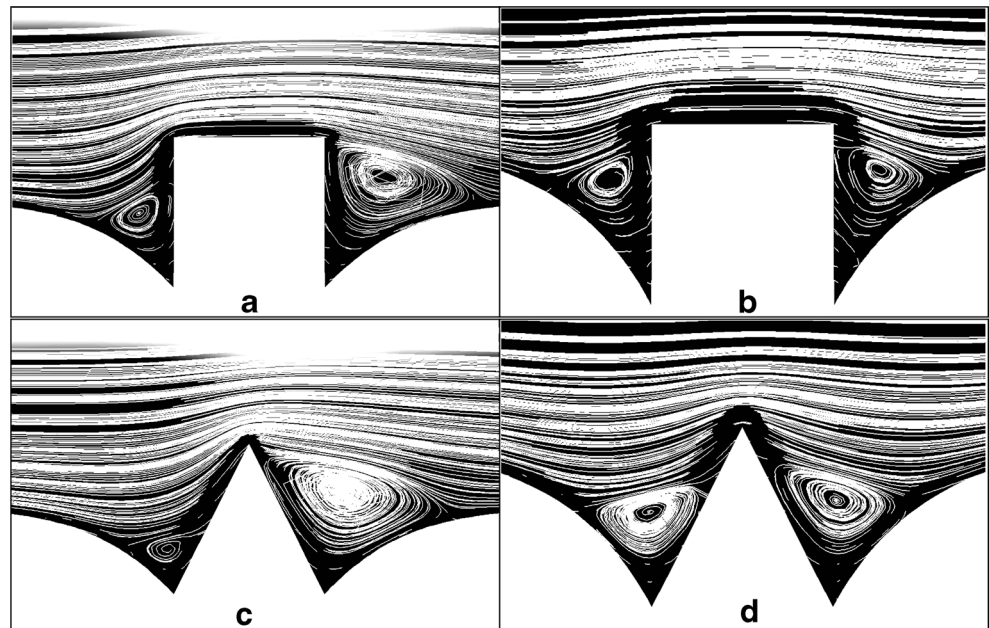
nondominated points in both cross sections are concentrated on the extreme left side of the  $\gamma$  and average stress curve in Fig. 9. From the nondominated sets, the corner point yields the best performance in minimization of  $\gamma$  and average stress. However, further investigation of the flow and mechanical physical conditions is needed.

## 4 Discussion

Based on the obtained surrogate model, we observe that for both cross-sectional cases, the configurations of small  $G$  and big  $SL$  strut is not recommended. Focusing on the  $\gamma$ -minimization surrogate model, broader areas with  $\gamma$  less than 40% are



**Fig. 10** Flow patterns near rectangular strut configuration of **a**  $G$ - $SL$  1.5–0.32 mm and **b**  $G$ - $SL$  1.19–0.17 mm. Flow patterns near triangular strut configuration of **c**  $G$ - $SL$  1.5–0.32 mm and **d**  $G$ - $SL$  1.19–0.17 mm



produced by the triangular strut. In addition, due to the different  $\gamma$  values suggested by each cross section in particular on  $G$ - $SL$  1.5–0.32 mm and  $G$ - $SL$  1.19–0.17 mm, thus we give special focus on these configurations. The flow patterns for both cross-sectional shapes are shown in Fig. 10 with each recirculation zone (RCZ) length listed in Table 2. Shorter RCZs are observed with the triangular strut, which produces smaller  $\gamma$  (%) near the strut [30]; thanks to the smaller flow disturbance generated by triangular design owing to its streamlined shape.

For the second objective, both surrogate models produce similar general trend, in which the average stress increases with decreasing  $SL$ . Apparently, there is a trade-off between  $G$ - $SL$  configurations and the objectives. Past single objective optimization works [22, 23] has shown that small struts

minimize  $\gamma$  (%) because of the smaller flow disturbance owing to RCZ at the narrow strut–vessel gap and the wall deformation, whereas the rest of the blood vessel wall surface is exposed directly to the main flow. However, small struts are responsible for the high average stresses on the vessel surface because of the narrower contact surface area.

Regarding the nondominated sets for both cross sections, a wide average stress gap is observed in the nondominated solution of low  $\gamma$  between points d and e, and f and g for rectangular and triangular shapes, respectively. After checking the  $G$ - $SL$  configurations between these points (Table 1), the wide average stress gap is likely the result of the significant difference strut  $SL$  between nondominated points; points a, b, c, and d in Fig. 9a are distributed in the narrow region of low average stress with significantly different  $\gamma$  values. Based on the flow pattern of points a and d (Fig. 11), small RCZ is observed in point d which causes small  $\gamma$  values. In contrast, the narrow distribution of nondominated points corresponds to the triangular cross-sectional shape, in particular, points c, d, e, and f. The combination of similar  $SL$  (Table 1) and RCZ– $G$  ratios (Table 2) is the reason for this. For analysis based on nondeformed wall conditions, either the flow pattern or  $\gamma$  will differ [30]. From Fig. 11, we can also observe that the general tendency of the RCZ shape of rectangular struts is similar, as previously obtained by study of Jimenez, *et al.* in [40].

Previous studies have shown that the WSS condition is transferred through the endothelial cells to the smooth muscle cells (SMC). Therefore, the low WSS could trigger a phenotype change of SMC, which could cause the atherosclerotic plaque to grow [35]. In addition, excess mechanical stresses on the vessel surface may also promote cell inflammation owing to injury [9]. Hence, it is

**Table 2** RCZ length and ratio of RCZ and length of  $G$

	Nondominated point/case	Recirculation zone [RCZ] length (mm)	RCZ– $G$ ratio (%)
Rectangular strut	a	1.01	45.1
	d	0.71	26.3
	Case 2	0.55	36.7
	Case 24	0.15	12.6
Triangular strut	a	0.67	32.5
	c	0.74	27.5
	d	0.88	31.3
	e	0.9	30
	f	0.78	26
	Case 2	0.3	20
	Case 24	0.11	9.24

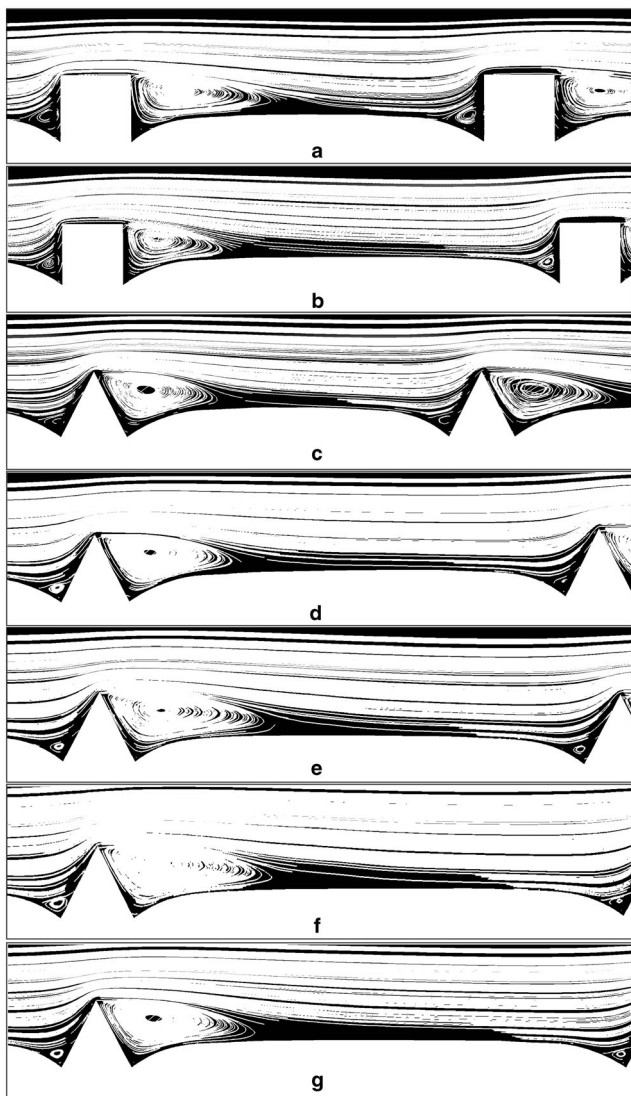


**Fig. 11** Flow patterns of extreme cases of nondominated solutions. **a, b** Rectangular nondominated point **a** and **d**, **c–f** triangular nondominated point **a**, **c**, **d**, **e**, **f**

important to balance the post deployment  $\gamma$  area and average stress on the blood vessel surface. Combinations of relatively big  $SL$  struts with long  $G$  are the best to satisfy both objective functions for rectangular and triangular struts. Further evaluation of cell behavior toward this optimized design is interesting to be investigated. Although strut with an exact parameter criteria are sometimes hard to be fabricated, the process of design exploration from the utilization of surrogate model contour map can be beneficial to solve the problem of fabrication constraint.

Several assumptions were applied to this work that put the simulation under some limitations. Although the real blood flow is pulsatile, we used steady flow assumption since it is efficient in terms of the computational cost. Moreover, our previous work shows that the difference between the surrogate model construction, which was derived

from pulsatile transient simulation, was insignificant [30]. We also treat the blood fluid as a Newtonian fluid, which may lead to some flaw simulation results, particularly, on the near-wall area where the non-Newtonian properties of blood are likely to appear. However, based on the Fahraeus–Lindqvist effect, this non-Newtonian effect begins to play a role on the vessel size with a diameter less than 1 mm [9]. For the solid mechanics domain, an assumption of simple linear mechanical model for blood vessels was applied. This assumption cannot appropriately represent the nonlinear and anisotropic behavior of the blood vessel, which comprises many layers of complex fibers [32, 41]. Therefore, more complex models of the intravascular environment and stent geometry with high-order design variables need to be considered. Although this simulation has shown the results with certain level of convergence from both meshes dependency and solver convergence, it is also important to increase the simulation accuracy by improving the computational resources to handle more mesh elements, especially for small struts. As the validation of this optimization study, future work on in vitro investigations of how the optimized solution will affect the cellular activities is also necessary, as is necessary to find the exact threshold of the best  $\gamma$  (%) and average stress for healthy vascular conditions.

## 5 Conclusions

In this study, 3D computational multiobjective optimization by minimizing low WSS ratio ( $\gamma$ ) and the average stress along the deployment area under deformed wall conditions for triangular and rectangular struts was performed. To balance both objectives, we suggest design configurations for  $G$ - $SL$  of 2.81–0.39 mm (rectangular nondominated point **d**) and 3.00–0.43 mm (triangular nondominated point **f**) for rectangular and triangular struts, respectively. The triangular strut is predicted to produce better intravascular hemodynamics; however, regarding the average stress, both strut types show no significant differences.

**Acknowledgments** We would like to thank Dr. Yasutomo Shimizu for his help and suggestions during the preparation of this manuscript.

**Funding information** This research is supported by Indonesia Endowment for Education Fund (LPDP), Ministry of Finance, Republic of Indonesia through *Beasiswa Pendidikan Indonesia* Scholarship Program for Doctorate Students and the ImPACT program of Council for Science, Technology and Innovation (Cabinet Office, Government of Japan).

## Compliance with ethical standards

**Conflict of interest** The authors declare that they have no conflict of interest.

## References

- Elmore JB, Mehanna E, Parikh SA, Zidar DA (2016) Restenosis of the coronary arteries: past, present, future directions. *Interv Cardiol Clin* 5:281–293. <https://doi.org/10.1016/j.iccl.2016.03.002>
- Giacoppo D, Gargiulo G, Aruta P, Capranzano P, Tamburino C, Capodanno D (2015) Treatment strategies for coronary in-stent restenosis: systematic review and hierarchical Bayesian network meta-analysis of 24 randomised trials and 4880 patients. *BMJ*: h5392. <https://doi.org/10.1136/bmj.h5392>
- Chen HY, Hermiller J, Sinha AK, Sturek M, Zhu L, Kassab GS (2009) Effects of stent sizing on endothelial and vessel wall stress: potential mechanisms for in-stent restenosis. *J Appl Physiol* 106: 1686–1691. <https://doi.org/10.1152/jappphysiol.91519.2008>
- Patel SM, Li J, Parikh SA (2016) Design and comparison of large vessel stents. *Interv Cardiol Clin* 5:365–380. <https://doi.org/10.1016/j.iccl.2016.03.005>
- Freeman JW, Snowhill PB, Noshier JL (2010) A link between stent radial forces and vascular wall remodeling: the discovery of an optimal stent radial force for minimal vessel restenosis. *Connect Tissue Res* 51:314–326. <https://doi.org/10.3109/03008200903329771>
- Otsuka F, Nakano M, Ladich E, Kolodgie FD, Virmani R (2012) Pathologic etiologies of late and very late stent thrombosis following first-generation drug-eluting stent placement. *Thrombosis* 2012:1–16. <https://doi.org/10.1155/2012/608593>
- Lewis G (2008) Materials, fluid dynamics, and solid mechanics aspects of coronary artery stents: a state-of-the-art review. *J Biomed Mater Res Part B Appl Biomater* 86B:569–590. <https://doi.org/10.1002/jbm.b.31028>
- Beier S, Ormiston J, Webster M, Cater J, Norris S, Medrano-Gracia P, Young A, Cowan B (2015) Hemodynamics in idealized stented coronary arteries: important stent design considerations. *Ann Biomed Eng* 44:315–329. <https://doi.org/10.1007/s10439-015-1387-3>
- Westerhof N, Stergiopulos N, Noble MIM (2010) Snapshots of hemodynamics
- Putra NK, Anzai H, Ohta M (2016) Hemodynamic behaviours under blood vessel deformation by stent struts: two dimensional study. In: Thirteenth International Conference on Flow Dynamics pp 294–295
- Mejia J, Ruzzeh B, Mongrain R, Leask R, Bertrand OF (2009) Evaluation of the effect of stent strut profile on shear stress distribution using statistical moments. *Biomed Eng Online* 8:8. <https://doi.org/10.1186/1475-925X-8-8>
- Chen Z, Zhan F, Ding J, Zhang X, Deng X (2016) A new stent with streamlined cross-section can suppress monocyte cell adhesion in the flow disturbance zones of the endovascular stent. *Comput Methods Biomech Biomed Eng* 19:60–66. <https://doi.org/10.1080/10255842.2014.984701>
- Srinivas K, Nakayama T, Ohta M, Obayashi S, Yamaguchi T (2008) Studies on design optimization of coronary stents. *J Med Device* 2:11004-1–11004-7
- Srinivas K, Townsend S, Lee C-J, Nakayama T, Ohta M, Obayashi S, Yamaguchi T (2010) Two-dimensional optimization of a stent for an aneurysm. *J Med Device* 4:21003-1–21003-7
- Anzai H, Falcone JL, Chopard B, Hayase T, Ohta M (2014) Optimization of strut placement in flow diverter stents for four different aneurysm configurations. *J Biomech Eng* 136:61006-1–61006-7
- Bressloff NW, Ragkousis G, Curzen N (2015) Design optimisation of coronary artery stent systems. *Ann Biomed Eng* 44:1–11. <https://doi.org/10.1007/s10439-015-1373-9>
- Zhang M, Anzai H, Chopard B, Ohta M (2016) Towards the patient-specific design of flow diverters made from helix-like wires: an optimization study. *Biomed Eng Online* 15(Suppl):371–382
- Li H, Gu J, Wang M, Zhao D, Li Z, Qiao A, Zhu B (2016) Multi-objective optimization of coronary stent using kriging surrogate model. *Biomed Eng Online* 15:148. <https://doi.org/10.1186/s12938-016-0268-9>
- Janiga G, Daróczy L, Berg P, Thévenin D, Skalej M, Beuing O (2015) An automatic CFD-based flow diverter optimization principle for patient-specific intracranial aneurysms. *J Biomech* 48:3846–3852. <https://doi.org/10.1016/j.jbiomech.2015.09.039>
- Kim YH, Xu X, Lee JS (2010) The effect of stent porosity and strut shape on saccular aneurysm and its numerical analysis with lattice Boltzmann method. *Ann Biomed Eng* 38:2274–2292. <https://doi.org/10.1007/s10439-010-9994-5>
- Li H, Liu T, Wang M, Zhao D, Qiao A, Wang X, Gu J, Li Z, Zhu B (2017) Design optimization of stent and its dilatation balloon using kriging surrogate model. *Biomed Eng Online* 16(13):13. <https://doi.org/10.1186/s12938-016-0307-6>
- Putra NK, Palar PS, Anzai H, et al (2017) Variation of strut parameter effects with wall deformation on stent deployment via surrogate model. In: 5th International Conference on Computational and Mathematical Biomed Eng pp 1007–1010
- Putra NK, Palar PS, Anzai H, et al (2018) Comparative Study Between Different Strut's Cross Section Shape on Minimizing Low Wall Shear Stress Along Stent Vicinity via Surrogate-Based Optimization. In: Schumacher A, Vietor T, Fiebig S, et al (eds) *Advances in Structural and Multidisciplinary Optimization: Proceedings of the 12th World Congress of Structural and Multidisciplinary Optimization (WCSMO12)*. Springer International Publishing, Cham, pp 2097–2109
- Yang XS, Koziel S, Leifsson L (2012) Computational optimization, modelling and simulation: smart algorithms and better models. In: *Procedia Computer Science*. Elsevier Masson SAS, pp 852–856
- AIJ F, Sobester A, Keane AJ (2008) *Engineering design via surrogate modelling*. Wiley., West-Sussex
- Kolar M, OS F (1993) Fast, portable and reliable algorithm for the calculation of Halton numbers. *Comput Math Appl* 25:3–13
- Otsuka F, Finn AV, Yazdani SK, Nakano M, Kolodgie FD, Virmani R (2012) The importance of the endothelium in atherothrombosis and coronary stenting. *Nat Rev Cardiol* 9:439–453. <https://doi.org/10.1038/nrcardio.2012.64>
- Mori F, Ohta M, Matsuzawa T (2015) Changes in blood flow due to stented parent artery expansion in an intracranial aneurysm. *Technol Health Care* 23:9–21. <https://doi.org/10.3233/THC-140871>
- Kono K, Shintani A, Terada T (2014) Hemodynamic effects of stent struts versus straightening of vessels in stent-assisted coil embolization for sidewall cerebral aneurysms. *PLoS One* 9:e108033. <https://doi.org/10.1371/journal.pone.0108033>
- Putra NK, Palar PS, Anzai H, et al (2017) Stent design optimization based on Kriging surrogate model under deformed vessel wall: pulsatile inlet flow. In: *ICA 2017 Proceedings*. IEEE
- Components JMM (2015) Nitinol technical properties. <http://jmmedical.com/resources/221/Nitinol-Technical-Properties.html>. Accessed 9 Sept 2015
- Fung YC (1996) *Blood flow in arteries*. In: *Biomechanics: circulation*, second. Springer-Verlag, New York, pp 108–205
- COMSOL Multiphysics (2014) *Fluid structure interaction in a network of blood vessels*. In: *Structural mechanics module model library manual*, vol 1, p 20
- Li Y, Anzai H, Nakayama T et al (2014) Simulation of hemodynamics in artery with aneurysm and stenosis with different geometric configuration. *J Biomech Sci Eng* 9:1–11. <https://doi.org/10.1299/jbse.2014jbse0003>
- Han X, Sakamoto N, Tomita N et al (2017) Influence of shear stress on phenotype and MMP production of smooth muscle cells in a coculture model. *J Biorheol* 31:50–56. <https://doi.org/10.17106/jbr.31.50>
- Chiastra C, Migliavacca F, Martínez MÁ, Malvè M (2014) On the necessity of modelling fluid-structure interaction for stented

- coronary arteries. *J Mech Behav Biomed Mater* 34:217–230. <https://doi.org/10.1016/j.jmbbm.2014.02.009>
37. Shimoyama K, Yoshimizu S, Jeong S et al (2011) Multi-objective design optimization for a steam turbine stator blade using LES and GA. *J Comput Sci Technol* 5:134–147. <https://doi.org/10.1299/jcst.5.134>
  38. Luo C, Shimoyama K, Obayashi S (2015) A study on many-objective optimization using the Kriging-surrogate-based evolutionary algorithm maximizing expected hypervolume improvement. *Math Probl Eng* 2015:1–15. <https://doi.org/10.1155/2015/162712>
  39. Emmerich MTM, Deutz AH, Klinkenberg JW (2011) Hypervolume-based expected improvement: monotonicity properties and exact computation. In: 2011 IEEE Congress of Evolutionary Computation, CEC 2011. pp 2147–2154
  40. Jimenez JM, Prasad V, Yu MD, Kampmeyer CP, Kaakour AH, Wang PJ, Maloney SF, Wright N, Johnston I, Jiang YZ, Davies PF (2014) Macro- and microscale variables regulate stent haemodynamics, fibrin deposition and thrombomodulin expression. *J R Soc Interface* 11:20131079–20131079. <https://doi.org/10.1098/rsif.2013.1079>
  41. Yeh HH, Rabkin SW, Grecov D (2017) Hemodynamic assessments of the ascending thoracic aortic aneurysm using fluid-structure interaction approach. *Med Biol Eng Comput* 56:1–17. <https://doi.org/10.1007/s11517-017-1693-z>



**Narendra Kurnia Putra** is a Ph.D. student in the Department of Bioengineering & Robotics, Graduate School of Engineering, Tohoku University, Japan. He was a research and academic assistant at Instrumentation and Control Research Group and Program Study of Engineering Physics, Faculty of Industrial Technology, Institut Teknologi Bandung, Bandung, Indonesia. Currently, he focuses his research on biofluid dynamics for stent optimization and its effect toward endothelial cells.



**Pramudita Satria Palar** obtained his Ph.D. from the Department of Aeronautics and Astronautics, University of Tokyo, Japan, in 2015. During his doctoral study, he was also a visiting researcher at Engineering Design Centre, University of Cambridge, UK, and wrote several collaborative papers with the centre. He is currently a research fellow at Tohoku University, Japan. His main research interests are fluid flow optimization, multiobjective optimization, and uncertainty

quantification in fluid dynamics.



**Hitomi Anzai** is an assistant professor in the Institute of Fluid Science, Tohoku University, Japan. She has received her Ph.D. at Tohoku University in 2014, working on automatic optimization of cerebral stent. Now, her fields are computational fluid dynamics for bioengineering and structural optimization.



**Koji Shimoyama** is an associate professor in the Institute of Fluid Science, Tohoku University, Japan. He obtained his Ph.D. from the Department of Aeronautics and Astronautics, University of Tokyo, Japan, in 2006. Previously, he was a research assistant at JAXA, a research fellow at Tohoku University, a visiting scholar at Stanford University, USA, and an invited Professor at Ecole Centrale De Lyon, France. His research interests are multiobjective design exploration, robust design optimization, and uncertainty quantification.



**Makoto Ohta** got his Ph.D. at Kyoto University, Japan, in 2001 and moved to Geneva University as a post-doctoral fellow in 2001. He developed an intracranial aneurysmal model using PVA-H with elasticity for evaluation of stent. And he also started Computational Fluid Dynamics of blood flow in intracranial aneurysm.

He got a position of Associate professor of Tohoku University, Institute of Fluid Science in 2005 and became professor of the institute in 2017. He published more than 100 papers and developed the field of evaluation of medical devices using model. He made a standard of mechanical properties of bone model in 2017 in ISO. He got frequently award, for example, best presentation award from Intracranial stent meeting (ICS) in 2012.